Nitrogen-doped carbon dots decorated on g-C₃N₄/Ag₃PO₄ photocatalyst with improved visible light photocatalytic activity and mechanism insight

Xuli Miao[a], Xiaoyang Yue[a], Zhenyuan Ji[a], Xiaoping Shen[a,*], Hu Zhou[b], Miaomiao Liu[a], Keqiang Xu[a], Jun Zhu[a], Guoxing Zhu[a], Lirong Kong[a], S.A. Shah[a]

[a] *School of Chemistry and Chemical Engineering, Jiangsu University, Zhenjiang 212013, People's Republic of China*
[b] *School of Material Science and Engineering, Jiangsu University of Science and Technology, Zhenjiang 212003, People's Republic of China*

ABSTRACT

In this work, an all solid Z-scheme g-C₃N₄/Ag₃PO₄/NCDs photocatalyst has been prepared through decorating the direct Z-scheme g-C₃N₄/Ag₃PO₄ photocatalyst with nitrogen-doped carbon dots (NCDs). The g-C₃N₄/Ag₃PO₄/NCDs photocatalyst exhibits excellent photocatalytic activity for the degradation of methylene blue (MB), rhodamine B (RhB) and phenol under visible light irradiation. The solutions of MB ($10 \, mg \, L^{-1}$) and RhB ($10 \, mg \, L^{-1}$) can be efficiently degraded within 20 min and 15 min, respectively, and the phenol ($50 \, mg \, L^{-1}$) can be degraded to 36% within 80 min, which are much better than those of Ag₃PO₄ and g-C₃N₄/Ag₃PO₄, indicating that the introduction of NCDs into g-C₃N₄/Ag₃PO₄ can effectively improve the photocatalytic activity. Moreover, the photocatalytic performance of g-C₃N₄/Ag₃PO₄/NCDs shows just a slight decrease after four degradation cycles, indicating a high stability of the g-C₃N₄/Ag₃PO₄/NCDs photocatalyst. A possible photocatalytic mechanism based on the experimental results is proposed. It is revealed that NCDs on the ternary g-C₃N₄/Ag₃PO₄/NCDs can enhance the light harvesting capacity and molecular oxygen activation ability of the photocatalyst, and serve as excellent electronic transmission medium to promote the transfer and separation of photo-generated electron-hole pairs. This study demonstrates that NCDs decorated photocatalysts are very promising for environment and related applications.

1. Introduction

Over the past decades, the increasing development of industry has brought about various environmental problems, especially the water pollution has been a serious challenge [1]. Semiconductor photocatalysis is one of the most important technologies for purifying wastewater because it can utilize the sunlight to decompose various organic pollutants [2]. However, single-component semiconductor photocatalysts always face various defects such as the low visible-light utilization and the easy recombination of photogenerated charge carriers. The construction of semiconductor heterostructures has been demonstrated to be highly effective for improving the photocatalytic efficiency [3]. Recently, a new type of semiconductor hetero-photocatalysts called all-solid-state Z-scheme photocatalysts has been applied to the photocatalysis owing to its unique advantage [4–7]. The all-solid-state Z-scheme photocatalysts are usually composed of two different semiconductors and an electron shuttle mediator such as Ag, Au, Pt and graphene [4,8–11]. When the Z-scheme photocatalysts are irradiated, the electrons in valence band (VB) of a semiconductor are firstly excited

to its conduction band (CB) to form photogenerated electrons with reducibility, and then the photogenerated electrons from the lower CB and the photogenerated holes from the higher VB are recombined through the electron mediator. As a result, the photogenerated electrons with a stronger reduction capacity in the higher CB and the photogenerated holes with a stronger oxidation capacity in the lower VB participate in the reduction and oxidation process in the photocatalytic degradation. This process is beneficial for simultaneously possessing high charge-separation efficiency and strong redox ability, and thus improves the photocatalytic efficiency.

Recently, the metal-free semiconductor of graphitic carbon nitride (g-C₃N₄) has attracted great attention in photocatalysis community because of its suitable band gap (2.7 eV), low cost and favorable thermal and chemical stability [12–16]. Nevertheless, due to the fast charge recombination, low electrical conductivity and the poor visible-light absorption (< 460 nm), the practical photocatalytic application of g-C₃N₄ is still hindered [17]. Silver orthophosphate (Ag₃PO₄) is a well-known visible-light-driven photocatalyst [18–22]. It was reported that when g-C₃N₄ was combined with Ag₃PO₄, the resulted g-C₃N₄/Ag₃PO₄

photocatalysts exhibited significantly enhanced photocatalytic activity. For example, Yang [23] and He [24] prepared g-C_3N_4/Ag/Ag_3PO_4 Z-Scheme photocatalysts with excellent photocatalytic properties. Chen [25] and Meng [26] reported that g-C_3N_4/Ag_3PO_4 in itself is a direct Z-Scheme photocatalyst, and exhibits enhanced photocatalytic performance. Nevertheless, despite the significant efforts, there still exist several challenges and problems in the direct Z-Scheme g-C_3N_4/Ag_3PO_4 photocatalytic heterojunction: (i) The utilization of visible light is not high enough, which limits its photocatalytic performance [27]; (ii) Some defects formed between g-C_3N_4 and Ag_3PO_4 could serve as the recombination centers for the electron-hole pairs, reducing the photocatalytic efficiency [28]; (iii) The molecular oxygen activation ability is not strong enough, which also restrains its photocatalytic activity [29].

Carbon dots (CDs) are a novel and ecofriendly zero-dimensional nano-carbon material, which is primarily composed of graphitic carbon (sp^2 carbon) with a size below 10 nm. CDs have attracted considerable attention because of their unique optical and electronic properties. On one hand, CDs exhibit excellent electron transfer and electron reservoir properties. They show satisfactory performances as a catalyst component or a cocatalyst [30,31]. On the other hand, CDs show upconversion photoluminescence properties. When CDs coupled with other semiconductors such as g-C_3N_4 [32], TiO_2 [33], ZnO [34], the composites could absorb a longer wavelength visible light and then emit a shorter wavelength ultraviolet light. As a result, the photocatalysts could produce more photogenerated charge carriers, and thus improve the photocatalytic efficiency. In addition, the optical and electrical properties of CDs can be tuned by doping with N atoms owing to the relatively strong electron affinity of N atoms [35]. The electrons in the CB of a semiconductor can easily transfer to N-doped carbon dots (NCDs), leading to the efficient separation of electron-hole pairs. Moreover, the doping with N atoms can lower the work function of CDs [35], leading to the enhancement of the photocatalytic performance. In this paper, we report a new all solid Z-scheme photocatalyst of g-C_3N_4/Ag_3PO_4/NCDs with NCDs as excellent light absorber and electronic transmission medium. The photocatalytic activity of the as-prepared photocatalyst is evaluated by the degradation of three different kinds of pollutants under visible light irradiation, and the possible photocatalytic mechanism of g-C_3N_4/Ag_3PO_4/NCDs is proposed.

2. Experimental section

2.1. Chemicals

All the chemical reagents employed in this study were obtained from Sinopharm Chemical Reagent Co. Ltd, which are of analytical-grade, and used as received without further purification. The water used in the experiment is deionized (DI) water.

2.2. Syntheses

2.2.1. Preparation of NCDs

The NCDs aqueous dispersion was prepared by a previously reported method [36]. Specifically, 5 mmol of citrate acid was dissolved in 10 mL of water containing 335 μL ethylenediamine. The above solution was then transferred to a 25 mL Teflon-lined autoclave and heated at 200 °C for 5 h. The product was subjected to dialysis for 24 h in order to remove the impurities, and then NCDs were obtained by freeze drying. The obtained NCDs were re-dispersed in water to prepare NCDs aqueous dispersion (1 mg/mL), which was stored at 4 °C for later use.

2.2.2. Preparation of g-C_3N_4 nanosheets

The bulk g-C_3N_4 was prepared by a simple calcination approach according to the literature [37,38]. Typically, 10 g of urea powder was put into an alumina crucible with a cover, and successively heated at 250 °C for 1 h, 350 °C for 1 h and 550 °C for 2 h with a heating rate of 2 °C min^{-1} in air atmosphere. Subsequently, the obtained bulk g-C_3N_4

was thermally exfoliated into g-C_3N_4 nanosheets by calcination at 600 °C for 2 h at air atmosphere. The faint yellow product was collected and then grounded into powder with an agate mortar for further use.

2.2.3. Preparation of g-C_3N_4/Ag_3PO_4

In a typical synthesis, 50 mg of the as-prepared g-C_3N_4 nanosheets was dispersed in 80 mL of DI water by ultrasonication. After that, 12.2 mL of $AgNO_3$ (100 mg mL^{-1}) aqueous solution was dropwise added to the suspension, and magnetically stirred for 6 h to enable sufficient adsorption of Ag$^+$ ions on the surface of g-C_3N_4 nanosheets. Finally, 10 mL of Na_2HPO_4 solution (100 mg mL^{-1}) was dripped into the reaction system under magnetic stirring, and the mixture was continuously stirred for another 6 h. The final product was collected by centrifugation, washed three times with DI water and ethanol, respectively, and then dried in vacuum at 45 °C for 12 h. Finally, the product was collected and then grounded into powder with an agate mortar for further use. The as-prepared sample is also denoted as g-C_3N_4/Ag_3PO_4-5 based on the feeding mass ratio (5:100) of g-C_3N_4 to Ag_3PO_4 in the preparation process.

2.2.4. Preparation of g-C_3N_4/Ag_3PO_4/NCDs

In a typical synthesis, 100 mg of the as-prepared g-C_3N_4/Ag_3PO_4 was dispersed in 80 mL of DI water with ultrasonication, afterwards a certain amount of NCDs aqueous dispersion (1 mg mL^{-1}) was added in and stirred for 24 h to enable NCDs decorated on the surface of g-C_3N_4 nanosheets and Ag_3PO_4 sufficiently. Finally, the product was collected by centrifugation, washed three times with DI water and ethanol, respectively, and then dried in vacuum at 45 °C for 12 h. The obtained samples were denoted as g-C_3N_4/Ag_3PO_4/NCDs-1, g-C_3N_4/Ag_3PO_4/NCDs-2, g-C_3N_4/Ag_3PO_4/NCDs-3 (or g-C_3N_4/Ag_3PO_4/NCDs), g-C_3N_4/Ag_3PO_4/NCDs-4 and g-C_3N_4/Ag_3PO_4/NCDs-5 for the NCDs feeding amount of 0.2, 0.5, 1, 2 and 5 mg, respectively. The preparation process of the g-C_3N_4/Ag_3PO_4/NCDs nanocomposites is depicted in Scheme 1.

For comparison, Ag_3PO_4 was prepared by directly mixing $AgNO_3$ and Na_2HPO_4 aqueous solutions in the absence of NCDs and g-C_3N_4. The g-C_3N_4/NCDs sample was prepared by mixing NCDs and g-C_3N_4 aqueous dispersions with a mass ratio of NCDs to g-C_3N_4 about 1: 100. Ag_3PO_4/NCDs composite was prepared by the same method as the g-C_3N_4/Ag_3PO_4 just substituting NCDs for g-C_3N_4 in the synthesis, and the mass ratio of NCDs to Ag_3PO_4 is about 1: 100.

2.3. Characterization of the photocatalysts

The phase structures of the as-prepared samples were investigated by X-ray diffraction (XRD, Bruker D8 ADVANCE) with Cu-K_α radiation ($\lambda = 1.5406$ Å) at a scanning rate of 7° min^{-1}. The morphology and sizes of the samples were observed by transmission electron microscopy (TEM, JEM-2100). Ultraviolet-visible (UV–vis) diffuse reflectance spectroscopy was performed using a UV–vis spectrophotometer (Shimadzu UV-2450, Japan) in the range of 200–800 nm by using $BaSO_4$ as a reflectance standard material. The infrared absorption spectra were recorded by a Fourier transform infrared spectrometer (FT-IR, Nicolet Nexus 470). The X-ray photoelectron spectroscopy (XPS) measurements were conducted on a Thermo ESCALAB 250XI spectrometer. The electron spin resonance (ESR) signals of radicals spin-trapped by spin-trap reagent 5,5-dimethyl-1-pyrroline N-oxide (DMPO) were recorded at 77 K with an ESR spectrometer (Bruker EPR A300-10/12) under the irradiation of a 500 W mercury lamp. Thermogravimetric analysis (TGA) was conducted by an integrated thermal analyzer (NETZSCH STA449C) at a heating rate of 10 °C min^{-1} in air. The transient photoluminescence (PL) decay spectra were recorded on an Edinburgh PLS980 spectrometer at room temperature.

2.4. Photocatalytic measurement

The photocatalytic activities of the as-prepared samples were
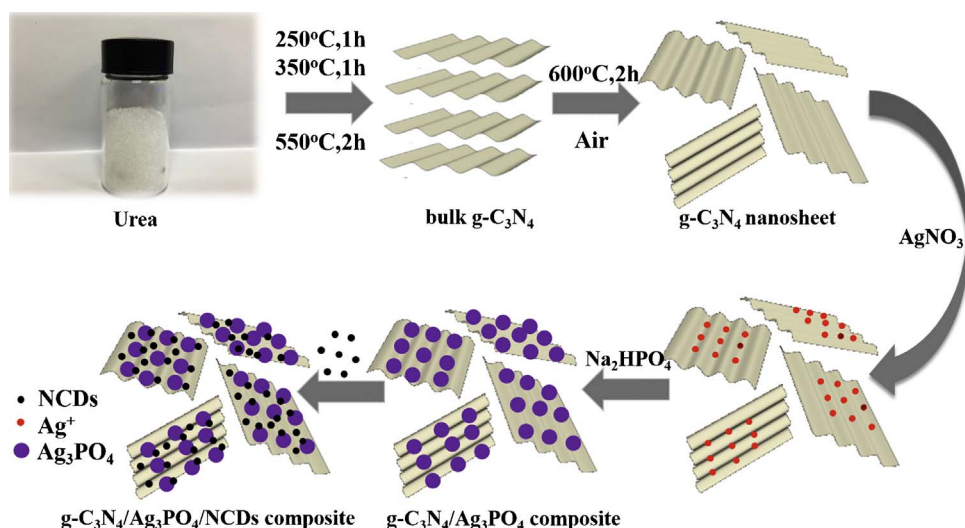
Scheme 1. Schematic illustration of the preparation process for g-C_3N_4/Ag_3PO_4/NCDs nanocomposites.

evaluated by the photocatalytic degradation of MB, RhB and phenol under visible-light irradiation. The photodegradation experiments were conducted on a GHX-3 photochemical reactor (Science and Education Equipment Co., Ltd, Yangzhou, China). A 250 W Xe lamp with a 420 nm cutoff filter was used as the visible light source. There is a water layer between the reaction system and the light source to remove thermal effect of light. The light intensity on the surface of the reaction mixture is *ca.* 256.4 mW/cm^2, estimated with a radiometer (FZ-A, China). In a typical experiment, 30 mg of the as-prepared photocatalyst was dispersed in 60 mL of MB (10 mg L^{-1}) or RhB (10 mg L^{-1}) aqueous solution. For the degradation of phenol, the dosage of the catalyst is 50 mg and it was dispersed in 50 mL of phenol (50 mg L^{-1}) aqueous solution. All the experiments were performed at room temperature under constant stirring. Prior to irradiation, the reaction mixture was magnetically stirred in the dark for 1 h to achieve an adsorption–desorption equilibrium between the photocatalyst and the pollutant (Fig. S1). During the photocatalytic process, 3 mL of the suspension was withdrawn at regular intervals and centrifuged, and then the supernatant was analyzed to determine the residual concentration of the pollutant by an UV–vis spectrophotometer. The characteristic absorption wavelengths of MB, RhB and phenol are 664 nm, 554 nm and 270 nm, respectively. In the recycle experiment, the photocatalyst was separated from reaction system and washed with ethanol and deionized water before being re-dispersed in the fresh MB solution for another cycle. Total organic carbon (TOC) was measured using a TOC analyzer (Analytik Jena AG multi N/C 2100). The degree of mineralization was calculated based on the TOC percent removal rate according to the expression:

$$Mineralization = (TOC_0\text{-}TOC_t)/TOC_0$$

Where TOC_0 is the concentration of TOC at $t = 0$ and TOC_t is its value at irradiation time t (min). All experiments were carried out in duplicate and only the mean values were reported.

2.5. Photoelectrochemical (PEC) measurement

An CHI 760D electrochemical workstation (ChenHua Instruments, Shanghai, China) with a standard three-electrode system was used to perform the electrochemical measurements. The platinum wire and saturated Ag/AgCl electrode were used as the counter electrode and the reference electrode, respectively. The 0.5 M Na_2SO_4 aqueous solution was used as the electrolyte. The working electrode was prepared by spreading as-prepared photocatalyst onto fluorine-doped tin oxide (FTO) glass with a light irradiation area of 1.0 cm^2. Typically, 4 mg of the as-prepared samples was dispersed in a mixed solution of 980 μL of

ethanol and 20 μL of Nafion by sonication to form a homogeneous suspension. Then 0.1 mL of the above suspension was coated onto FTO glass sheet and dried at 45 °C overnight to ensure the samples tightly attached on the FTO. A 300 W Xe lamp with a 420 nm cutoff filter was utilized as the visible light source, and the distance between illumination source and the photoelectrode was fixed to be 25 cm. The light intensity for PEC measurement is *ca.* 163.6 mW/cm^2. Electrochemical impedance spectra (EIS) were measured in 0.1 M KCl solution containing 2.5 mM $K_3[Fe(CN)_6]$/$K_4[Fe(CN)_6]$ (1:1) with a sinusoidal *ac* perturbation of 5 mV over a frequency range of 100 kHz to 100 mHz.

3. Results and discussion

3.1. Characterization of the as-prepared samples

Fig. 1a shows the XRD patterns of the as-prepared g-C_3N_4, Ag_3PO_4, g-C_3N_4/Ag_3PO_4 and g-C_3N_4/Ag_3PO_4/NCDs. For g-C_3N_4, a strong peak appears at 27.7°, which can be indexed to the (002) facet of g-C_3N_4 and is a characteristic interlayer-stacking peak of the C−N melon networks [11,38]. For pure Ag_3PO_4, all the diffraction peaks can be indexed to the cubic phase Ag_3PO_4 (JCPDS No. 06-0505). The XRD pattern of the NCDs (Fig. S2) displays a broad peak centered at *ca.* 25°, which can be attributed to the highly disordered carbon atoms [39]. The g-C_3N_4/Ag_3PO_4 and g-C_3N_4/Ag_3PO_4/NCDs show similar XRD patterns, and the characteristic peak of g-C_3N_4 was not observed in the patterns of g-C_3N_4/Ag_3PO_4 and g-C_3N_4/Ag_3PO_4/NCDs, which can be ascribed to the low contents and poor crystallinity of the well-exfoliated g-C_3N_4 in the composites as compared to those of Ag_3PO_4. Similar phenomena have been reported in many literatures [17,40]. As shown in Table S1, the contents of carbon and nitrogen from elemental analysis and the content of Ag from ICP analysis are well consistent with the expected compositions of the samples. And in both g-C_3N_4/Ag_3PO_4 and g-C_3N_4/Ag_3PO_4/NCDs, the contents of NCDs and g-C_3N_4 are quite low compared to that of Ag_3PO_4, in accordance with the fact that the characteristic peaks of NCDs and g-C_3N_4 were not observed in the XRD patterns of g-C_3N_4/Ag_3PO_4 and g-C_3N_4/Ag_3PO_4/NCDs. Fig. 1b shows the Raman spectra of the as-prepared Ag_3PO_4, NCDs, g-C_3N_4 and g-C_3N_4/Ag_3PO_4/NCDs. The Raman spectrum of Ag_3PO_4 shows two sharp peaks at 905 and 1000 cm^{-1}, which derive from the vibration of terminal oxygen of phosphate group [41]. The Raman spectrum of NCDs displays two prominent peaks at approximately 1375 and 1580 cm^{-1}, which correspond to the D and G bands of carbon-based materials [30]. For the Raman spectrum of g-C_3N_4, two weak peaks are observed at 1232 cm^{-1} and 1481 cm^{-1}, respectively, which are related to the vibration modes of CN heterocycles [42,43]. Meanwhile,
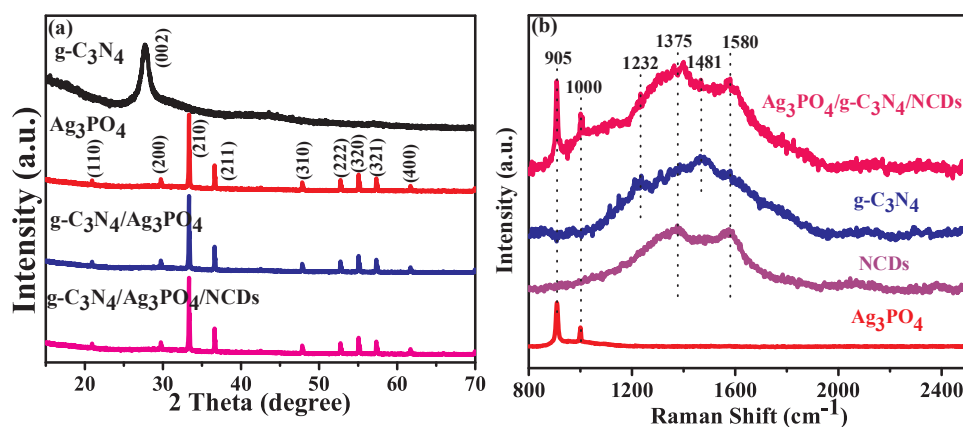
Fig. 1. (a) XRD patterns of the as-prepared g-C$_3$N$_4$, Ag$_3$PO$_4$, g-C$_3$N$_4$/Ag$_3$PO$_4$ and g-C$_3$N$_4$/Ag$_3$PO$_4$/NCDs. (b) Raman spectra of the as-prepared Ag$_3$PO$_4$, NCDs, g-C$_3$N$_4$ and g-C$_3$N$_4$/Ag$_3$PO$_4$/NCDs.

compared to bulk g-C$_3$N$_4$ with a bunch of peaks in the range of 1200–1600 cm^{-1} [44], the as-prepared g-C$_3$N$_4$ mainly exhibits a wide band in this region, which further suggests that the bulk g-C$_3$N$_4$ has been well exfoliated to thin g-C$_3$N$_4$ nanosheets [42]. For the Raman spectrum of g-C$_3$N$_4$/Ag$_3$PO$_4$/NCDs, all characteristic peaks from Ag$_3$PO$_4$, NCDs, g-C$_3$N$_4$ can be detected, indicating the successful combination of g-C$_3$N$_4$, NCDs and Ag$_3$PO$_4$ in the composite.

The exact compositions of the as-prepared samples are investigated by thermogravimetric (TG) analysis. As shown in TG curves (Fig. S3), the Ag$_3$PO$_4$ sample shows no obvious weight loss from room temperature to 800 °C, which is consistent with previous report [45]. The decomposition temperatures of the g-C$_3$N$_4$/Ag$_3$PO$_4$ and g-C$_3$N$_4$/Ag$_3$PO$_4$/NCDs composites are obviously lower than that of pure g-C$_3$N$_4$, suggesting the catalytic action of Ag$_3$PO$_4$ for g-C$_3$N$_4$ oxidation [45]. In the g-C$_3$N$_4$/Ag$_3$PO$_4$ and g-C$_3$N$_4$/Ag$_3$PO$_4$/NCDs composites, the remnant weights of approximately 95 wt.% and 94.5 wt.% could be ascribed to the presence of Ag$_3$PO$_4$, which are consistent with the contents of Ag$_3$PO$_4$ in the g-C$_3$N$_4$/Ag$_3$PO$_4$ and g-C$_3$N$_4$/Ag$_3$PO$_4$/NCDs composites (Table S1).

The typical TEM images of as-prepared g-C$_3$N$_4$, NCDs, Ag$_3$PO$_4$, g-C$_3$N$_4$/Ag$_3$PO$_4$ and g-C$_3$N$_4$/Ag$_3$PO$_4$/NCDs are shown in Fig. 2. As shown in Fig. 2a, it can be seen that the g-C$_3$N$_4$ shows thin wrinkled nanosheet structure, which could possess larger specific surface area and more reactive sites than bulk g-C$_3$N$_4$ after the thermal exfoliation. Fig. 2b shows the TEM image of the nitrogen-doped carbon dots, which illustrates that the as-prepared NCDs are highly monodispersed with a narrow size distribution of 2.5–4.5 nm (Fig. S4), well consistent with the literature report [36]. The pristine Ag$_3$PO$_4$ presents as irregular particles with a size of 200–600 nm (Fig. 2c). As can be seen from Fig. 2d–f, in g-C$_3$N$_4$/Ag$_3$PO$_4$ and g-C$_3$N$_4$/Ag$_3$PO$_4$/NCDs composites, Ag$_3$PO$_4$ particles with a similar size were well anchored on the surface of g-C$_3$N$_4$. In addition, some small-sized NCDs were anchored on both g-C$_3$N$_4$ and Ag$_3$PO$_4$ in the g-C$_3$N$_4$/Ag$_3$PO$_4$/NCDs composite (Figs. Figure 2f and S5), which could serve as the electron mediator between g-C$_3$N$_4$ and Ag$_3$PO$_4$, and accelerate the separation of electron-hole pairs in photocatalytic process.

XPS analysis was conducted to investigate the surface composition and chemical states of the as-prepared samples. XPS spectra of NCDs, g-C$_3$N$_4$/Ag$_3$PO$_4$, Ag$_3$PO$_4$/NCDs, g-C$_3$N$_4$/NCDs and g-C$_3$N$_4$/Ag$_3$PO$_4$/NCDs are shown in Fig. 3 and Figs. S6–S9. From the XPS survey spectra in Figs. S6a and S7a, the elements of C, N and O were detected in both NCDs and g-C$_3$N$_4$/NCDs, and the molar ratio of C:N:O in NCDs is about 2.6:2:1, further confirming the N doping in the carbon dots. From the XPS survey spectra in Figs. Figure 3a, S8a and S9a, the elements of C, N, O, Ag and P were detected in Ag$_3$PO$_4$/NCDs, g-C$_3$N$_4$/Ag$_3$PO$_4$ and g-C$_3$N$_4$/Ag$_3$PO$_4$/NCDs, which are consistent with the compositions of these composites. Fig. 3b shows the high-resolution O 1s spectrum, and the three deconvoluted peaks at 530.4 eV, 531.6 eV and 532.6 eV can be ascribed to O^{-II}(Ag−O bond and P-O bond) in Ag$_3$PO$_4$ [46], the surface

OH-groups and the surface adsorbed H$_2$O molecules [47], respectively. The N 1s spectra of NCDs (Fig. S6c) and Ag$_3$PO$_4$/NCDs (Fig. S8c) can be deconvoluted into two peaks at 398.5 eV and 399.1 eV, respectively, which can be attributed to C−N=C and tertiary nitrogen (NC$_3$) in NCDs. While for g-C$_3$N$_4$/Ag$_3$PO$_4$, g-C$_3$N$_4$/NCDs, and g-C$_3$N$_4$/Ag$_3$PO$_4$/NCDs, the N 1s spectra of them can all be deconvoluted into three peaks. Besides the peaks at 398.5 eV and 399.1 eV, the peak at 400.7 eV can be found, which derives from the NH$_x$ groups in g-C$_3$N$_4$ [47]. The C 1s spectra of all the samples (Figs. Figure 3d, S6b–S9b) show three deconvoluted peaks at 284.8 eV, 286.2 eV and 288.4 eV, which can be ascribed to C−C bonds, hydroxylated surface carbon atoms (C−OH) and CN$_3$ bonds in the heterocycle ring of NCDs and g-C$_3$N$_4$, respectively [47]. However, the relative intensities of the C−C, C−OH and CN$_3$ peaks depend on the presence of NCDs and/or g-C$_3$N$_4$. The NCDs show the strongest C−C peaks, while the g-C$_3$N$_4$ exhibits the strongest CN$_3$ peaks. In Figs. Figure 3e, S8d and S9d, the Ag 3d$_{5/2}$ and Ag 3d$_{3/2}$ peaks at 368.4 eV and 374.4 eV can be ascribed to Ag$^+$ in Ag$_3$PO$_4$ [48], indicating that the same status of the silver ions in these samples. In addition, the P 2p spectrum (Fig. 3f) shows P 2p peaks at 132.8 eV, which is in good agreement with P^{+5} in Ag$_3$PO$_4$ [49].

The FT-IR spectra of the as-prepared samples are shown in Fig. 4a. The two peaks at 1010 cm^{-1} and 558 cm^{-1} in the FT-IR spectrum of Ag$_3$PO$_4$ is assigned to the P−O stretching vibration in PO$_4^{3-}$ [25,49]. In the FT-IR spectrum of g-C$_3$N$_4$, several strong peaks observed in 1200–1650 cm^{-1} correspond to the typical stretching modes of C−N and C=N heterocycles in g-C$_3$N$_4$ [50]. In addition, another sharp peak at 809 cm^{-1} is ascribed to the typical characteristic breathing mode of the tri-s-triazine units. In the FT-IR spectrum of NCDs, two peaks at 1056 and 1398 cm^{-1} are ascribed to the alkoxy C−O stretching and the bending mode of tertiary alcoholic C−OH groups, respectively, which are consistent with the previous reports [51]. For the g-C$_3$N$_4$/Ag$_3$PO$_4$ and g-C$_3$N$_4$/Ag$_3$PO$_4$/NCDs composites, all the characteristic peaks of g-C$_3$N$_4$ and Ag$_3$PO$_4$ are observed. However, the absorption peaks from NCDs are not observed in the g-C$_3$N$_4$/Ag$_3$PO$_4$/NCDs composite, which could be due to the low content of NCDs in the composite.

The UV–vis diffuse reflectance spectra of the as-prepared samples are depicted in Fig. 4b. For pristine g-C$_3$N$_4$ nanosheets, an absorption edge at about 460 nm was presented, indicating the band gap of g-C$_3$N$_4$ is 2.7 eV, which is consistent with previous results [38]. Compared to g-C$_3$N$_4$, pristine Ag$_3$PO$_4$ exhibits better visible-light absorption performance with an absorption edge at about 530 nm (band gap of 2.45 eV), which is in agreement with the result reported previously [52]. When NCDs are combined with g-C$_3$N$_4$/Ag$_3$PO$_4$, the g-C$_3$N$_4$/Ag$_3$PO$_4$/NCDs composite shows improved visible-light absorption compared to pristine Ag$_3$PO$_4$ and binary g-C$_3$N$_4$/Ag$_3$PO$_4$, which illustrates that the introduction of NCDs into the system enhances the visible light harvesting capacity. The strong visible-light absorption of NCDs (Fig. S10) stems from a variety of π-π* (C=C) and n-π* (C=O or C=N) transitions [53,54]. The phenomenon is agreed with the colors of the samples
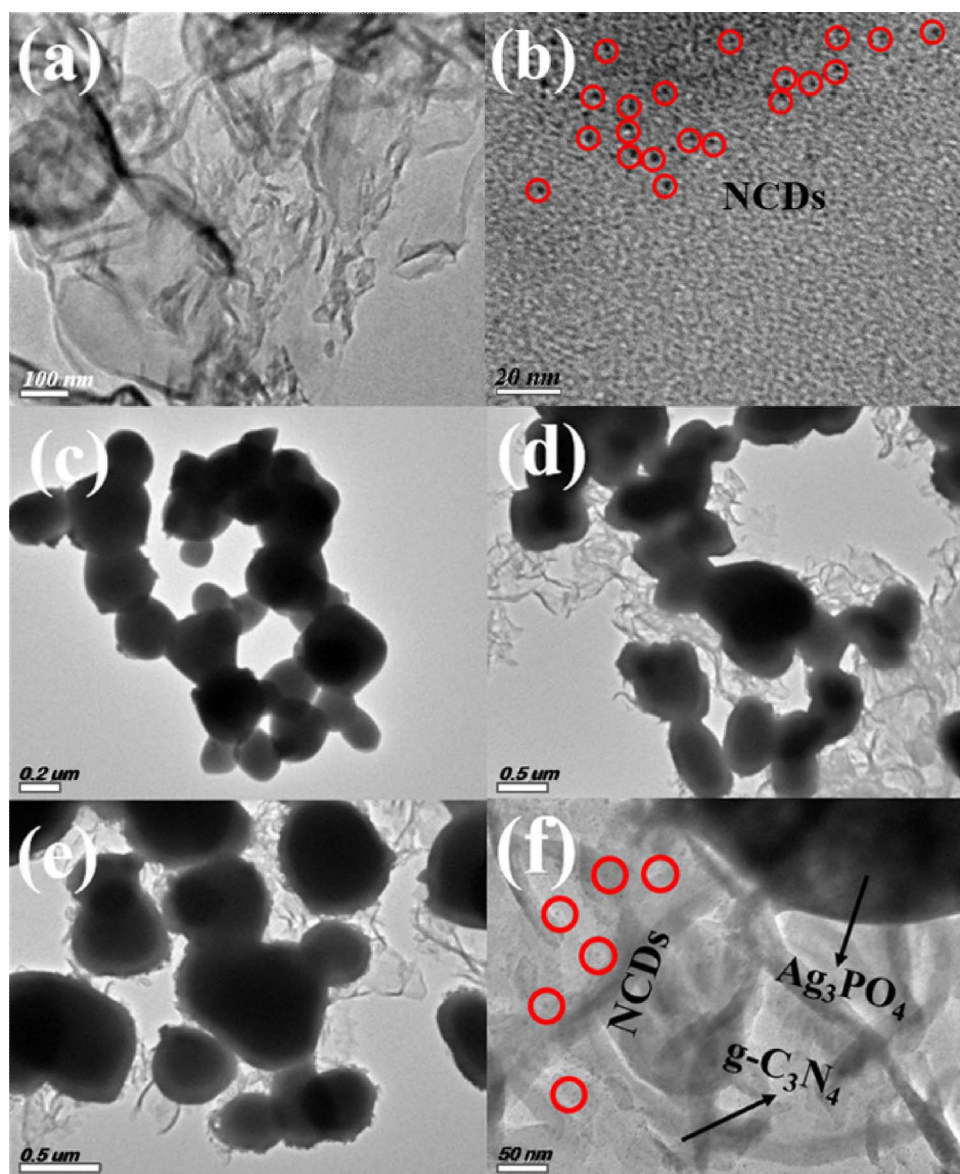
Fig. 2. TEM images of the as-prepared (a) g-C$_3$N$_4$, (b) NCDs, (c) Ag$_3$PO$_4$, (d) g-C$_3$N$_4$/Ag$_3$PO$_4$ and (e, f) g-C$_3$N$_4$/Ag$_3$PO$_4$/NCDs nanocomposite.

which change from light yellow to dark brown (see the insert in Fig. 4b).

3.2. Photocatalytic performances

The photocatalytic activities of the as-prepared samples were firstly evaluated by the degradation of MB as model pollutant under visible-light irradiation. As shown in Fig. S11, the binary g-C$_3$N$_4$/Ag$_3$PO$_4$ photocatalysts show enhanced photocatalytic performance compared to single g-C$_3$N$_4$ and Ag$_3$PO$_4$. With the increase of g-C$_3$N$_4$ content, the photocatalytic activities of g-C$_3$N$_4$/Ag$_3$PO$_4$ photocatalysts increase at first and then decrease. The g-C$_3$N$_4$/Ag$_3$PO$_4$-5 with mass ratio of g-C$_3$N$_4$ to Ag$_3$PO$_4$ about 5: 100 exhibits the best photocatalytic activity. On this basis, we added different amounts of NCDs into g-C$_3$N$_4$/Ag$_3$PO$_4$-5 to further optimize the photocatalytic performance. As displayed in Fig. 5a and b, after 40 min visible-light irradiation, the MB removal efficiencies over P25 (commercial TiO$_2$ photocatalyst), g-C$_3$N$_4$, g-C$_3$N$_4$/NCDs, Ag$_3$PO$_4$, Ag$_3$PO$_4$/NCDs, g-C$_3$N$_4$/Ag$_3$PO$_4$, g-C$_3$N$_4$/Ag$_3$PO$_4$/NCDs-1, g-C$_3$N$_4$/Ag$_3$PO$_4$/NCDs-2, g-C$_3$N$_4$/Ag$_3$PO$_4$/NCDs-3, g-C$_3$N$_4$/Ag$_3$PO$_4$/NCDs-4 and g-C$_3$N$_4$/Ag$_3$PO$_4$/NCDs-5 are 14%, 19%, 29%, 85%, 87%, 90%, 96%, 97%, 99%, 98% and 91%, respectively. This result indicates that the ternary composites of g-C$_3$N$_4$/Ag$_3$PO$_4$/NCDs show higher photocatalytic activity than single g-C$_3$N$_4$, Ag$_3$PO$_4$ as well as binary composites of g-C$_3$N$_4$/NCDs, Ag$_3$PO$_4$/NCDs and g-C$_3$N$_4$/Ag$_3$PO$_4$, and the g-C$_3$N$_4$/Ag$_3$PO$_4$/NCDs-3 sample exhibits the best photocatalytic degradation performance. As shown in Fig. S12a, the photocatalytic reaction rate can be described by the pseudo-first-order kinetic: $-\ln (C/C_0) = kt$, where t (min) is the irradiation time and k (min^{-1}) is the apparent reaction rate constant. It can be seen from Fig. S12b that g-C$_3$N$_4$/Ag$_3$PO$_4$/NCDs-3 possesses the highest rate constant (0.119 min^{-1}), which is about 39.6, 23.8, 14.8, 2.6, 2.3 and 1.6 times higher than that of P25 (0.003 min^{-1}), g-C$_3$N$_4$ (0.005 min^{-1}), g-C$_3$N$_4$/NCDs (0.008 min^{-1}), Ag$_3$PO$_4$ (0.046 min^{-1}), Ag$_3$PO$_4$/NCDs (0.051 min^{-1}) and g-C$_3$N$_4$/Ag$_3$PO$_4$ (0.074 min^{-1}). Obviously, the photocatalytic performance of the binary g-C$_3$N$_4$/Ag$_3$PO$_4$ can be further enhanced by the introduction of NCDs into the system. In addition, it is worth noting that with the increasing content of NCDs, the photocatalytic activity of the ternary g-C$_3$N$_4$/Ag$_3$PO$_4$/NCDs photocatalysts increases first and then decreases. Therefore, an appropriate amount of NCDs in the ternary photocatalysts is crucial for achieving the optimum photocatalytic efficiency. On one hand, too low content of NCDs in the composites cannot effectively promote the transfer of photogenerated charge carriers and improve the visible-light absorption, leading to a relatively low catalytic efficiency. On the other hand, too much NCDs
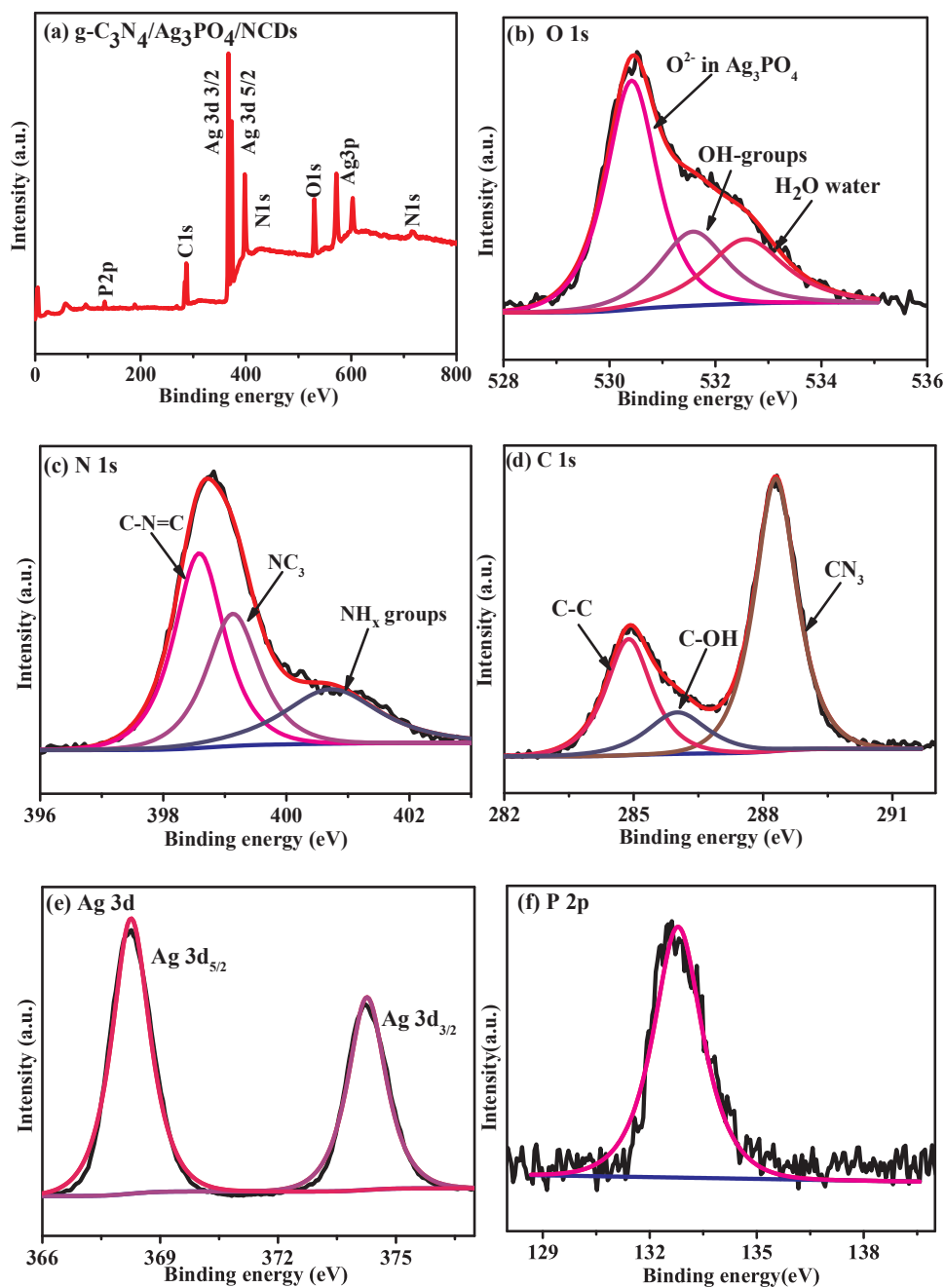
Fig. 3. (a) XPS survey spectrum and high-resolution XPS spectra of (b) O 1s, (c) N 1s, (d) C 1s, (e) Ag 3d and (f) P 2p for g-C_3N_4/Ag_3PO_4/NCDs nanocomposite.
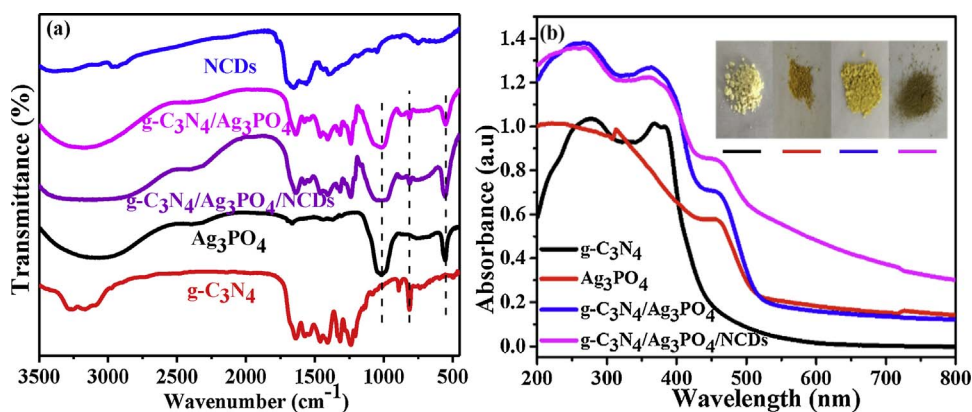
Fig. 4. (a) FT-IR spectra of the as-prepared Ag_3PO_4, g-C_3N_4, NCDs, g-C_3N_4/Ag_3PO_4 and g-C_3N_4/Ag_3PO_4/NCDs; (b) UV–vis diffuse reflectance spectra of g-C_3N_4, Ag_3PO_4, g-C_3N_4/Ag_3PO_4 and g-C_3N_4/Ag_3PO_4/NCDs. The inset in Fig. 4b displays the digital pictures of the as-prepared samples.
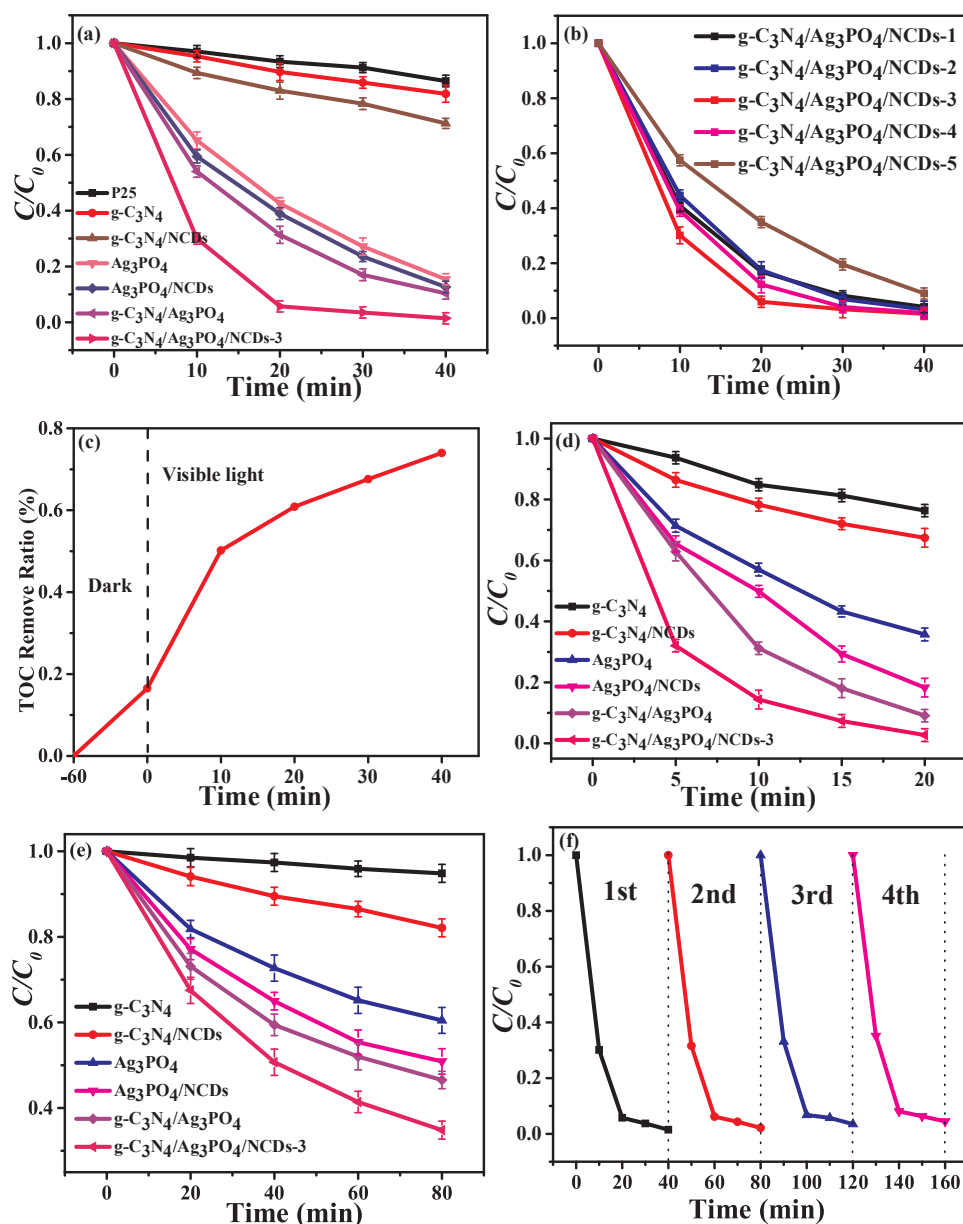
Fig. 5. (a, b) The photocatalytic degradation of MB based on the as-prepared samples; (c) The time-dependent TOC removal ratio with g-C$_3$N$_4$/Ag$_3$PO$_4$/NCDs-3 photocatalyst; The photocatalytic degradation of (d) RhB and (e) phenol based on the as-prepared samples; (f) Cycle experiments of g-C$_3$N$_4$/Ag$_3$PO$_4$/NCDs-3 for photocatalytic degradation of MB under visible-light irradiation.

inserted into the system possibly act as the recombination centers, which reduce the photocatalytic efficiency. Meanwhile, contaminant mineralization ability works as a vital parameter for photocatalytic performance evaluation. Therefore, the TOC removal efficiency of the as-prepared g-C$_3$N$_4$/Ag$_3$PO$_4$/NCDs-3 photocatalyst is also analyzed to confirm the mineralization involved in this photocatalytic degradation of MB. As shown in Fig. 5c, g-C$_3$N$_4$/Ag$_3$PO$_4$/NCDs-3 exhibits a TOC removal rate of 74% under the visible light irradiation for 40 min, which suggested that mineralization process occurred in the degradation of MB, and MB could be effectively photodegraded by the g-C$_3$N$_4$/Ag$_3$PO$_4$/NCDs-3 photocatalyst. To clarify the degradation process of MB, the MB solution after 40 min photocatalytic degradation was analyzed by GC–MS and ion chromatography. As shown in Fig. S13, the signals at $m/z = 112$, $m/z = 125$ and $m/z = 149$ were detected by GC–MS, which correspond to the intermediates of 5-nitrocyclohexa-1,3-diene, cyclohexa-3,5-diene-1,2-diol and 2-methylbenzo thiazole, respectively, during the MB degradation. As shown in Fig. S14, the ions SO$_4^{2-}$, NO$_3^-$, and Cl$^-$ were found by ion chromatography, indicating that MB molecules could be degraded into SO$_4^{2-}$, NO$_3^-$, and Cl$^-$ ions after the photocatalysis. Based on above experimental results, a

plausible degradation mechanism of MB is proposed (Fig. S15). Firstly, Cl$^-$ is ionized in aqueous solution, and then the loss of four −CH$_3$ connected to N proceeds due to their smaller bond dissociation energy [55,56]. Secondly, the C−S and C−N bonds in the middle ring, which are the more active parts, are broken into smaller molecular weight intermediates such as 5-nitrocyclohexa-1,3-diene, cyclohexa-3,5-diene-1,2-diol and 2-methylbenzo thiazole. Finally, the organic intermediates are further degraded into CO$_2$ and some inorganic ions such as SO$_4^{2-}$ and NO$_3^-$.

In order to further demonstrate the excellent visible-light photocatalytic performance of g-C$_3$N$_4$/Ag$_3$PO$_4$/NCDs, two typical pollutants of RhB and phenol were also degraded. As depicted in Fig. 5d, after 20 min visible-light irradiation, the RhB removal efficiencies over g-C$_3$N$_4$, g-C$_3$N$_4$/NCDs, Ag$_3$PO$_4$, Ag$_3$PO$_4$/NCDs, g-C$_3$N$_4$/Ag$_3$PO$_4$ and g-C$_3$N$_4$/Ag$_3$PO$_4$/NCDs-3 are about 26%, 33%, 65%, 82%, 91% and 99%, respectively. The result of the photocatalytic degradation of refractory pollutant phenol was shown in Fig. 5e. After 80 min visible-light irradiation, the phenol removal efficiencies over g-C$_3$N$_4$, g-C$_3$N$_4$/NCDs, Ag$_3$PO$_4$, Ag$_3$PO$_4$/NCDs, g-C$_3$N$_4$/Ag$_3$PO$_4$ and g-C$_3$N$_4$/Ag$_3$PO$_4$/NCDs-3 are about 6%, 18%, 40%, 50%, 53% and 64%, respectively, which
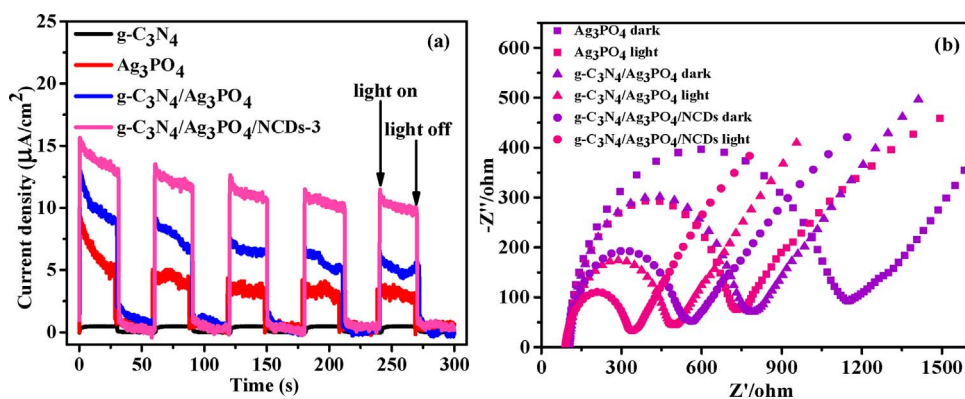
Fig. 6. (a) Transient photocurrent response curves of g-C$_3$N$_4$, Ag$_3$PO$_4$, g-C$_3$N$_4$/Ag$_3$PO$_4$ and g-C$_3$N$_4$/Ag$_3$PO$_4$/NCDs-3; (b) The electrochemistry properties of the as-prepared Ag$_3$PO$_4$, g-C$_3$N$_4$/Ag$_3$PO$_4$ and g-C$_3$N$_4$/Ag$_3$PO$_4$/NCDs samples: impedance spectra with the corresponding equivalent circuit models.

indicates the enormous potentiality of g-C$_3$N$_4$/Ag$_3$PO$_4$/NCDs photocatalyst for the degradation of organic dyes and other pollutants. In addition, the stability of a photocatalyst is also important to its practical application. As shown in Fig. 5f, the photocatalytic activity of g-C$_3$N$_4$/Ag$_3$PO$_4$/NCDs-3 for photocatalytic degradation of MB has no obvious decrease after four photodegradation cycles, demonstrating that the g-C$_3$N$_4$/Ag$_3$PO$_4$/NCDs photocatalyst has a high photocatalytic stability. The XRD and TEM results of the g-C$_3$N$_4$/Ag$_3$PO$_4$/NCDs-3 after 4 photocatalytic cycles are shown in Fig. S16a and Fig. S16b, respectively. From the XRD pattern, no evident crystalline structure change could be observed after photocatalysis, indicating the excellent stability of the g-C$_3$N$_4$/Ag$_3$PO$_4$/NCDs photocatalyst. It can be seen from the TEM image that after 4 photocatalytic cycles, the morphology and microstructure of the g-C$_3$N$_4$/Ag$_3$PO$_4$/NCDs remains almost the same as that of the fresh sample.

The photoelectrochemical analysis is a powerful technique to study the interfacial charge transfer and recombination rates for photocatalysts. Fig. 6a shows the transient photocurrent responses of g-C$_3$N$_4$, Ag$_3$PO$_4$, g-C$_3$N$_4$/Ag$_3$PO$_4$ and g-C$_3$N$_4$/Ag$_3$PO$_4$/NCDs-3 under intermittent visible-light irradiation for five on-off cycles. Obviously, the g-C$_3$N$_4$/Ag$_3$PO$_4$/NCDs-3 presents the highest photocurrent response among all these samples. This result indicates that the g-C$_3$N$_4$/Ag$_3$PO$_4$/NCDs composite possesses better separation efficiency for the photo-induced charge carriers than g-C$_3$N$_4$, Ag$_3$PO$_4$ and g-C$_3$N$_4$/Ag$_3$PO$_4$, demonstrating that carbon dots can efficiently boost the interfacial charge transfer and separation. To further demonstrate the importance of NCDs during the dynamic electron migration process, we also measured the time-resolved photoluminescence spectra of g-C$_3$N$_4$/Ag$_3$PO$_4$ and g-C$_3$N$_4$/Ag$_3$PO$_4$/NCDs [57]. As shown in Fig. S17, after fitting the curves with exponential model, the lifetime of g-C$_3$N$_4$/Ag$_3$PO$_4$ and g-C$_3$N$_4$/Ag$_3$PO$_4$/NCDs was obtained to be 7.25 ns and 8.12 ns, respectively. Compared with g-C$_3$N$_4$/Ag$_3$PO$_4$, g-C$_3$N$_4$/Ag$_3$PO$_4$/NCDs shows significantly prolonged lifetime. The longer lifetime may be attributed to the introduction of NCDs into the system, which accelerates the electron transfer and thus reduces the recombination of photoexcited electrons and holes, and typically, this is beneficial for photocatalytic and photocurrent reaction.

The improved charge transfer behavior of g-C$_3$N$_4$/Ag$_3$PO$_4$/NCDs was further validated by EIS measurement, the Nyquist plots of the Ag$_3$PO$_4$, g-C$_3$N$_4$/Ag$_3$PO$_4$ and g-C$_3$N$_4$/Ag$_3$PO$_4$/NCDs photoelectrodes in the dark and under visible-light radiation were presented in Fig. 6b. The semicircle part at the high frequency region is associated with the charge-transfer process at the photoelectrode interface, and a smaller radius implies more efficient charge transfer [58,59]. Consequently, a smaller arc of g-C$_3$N$_4$/Ag$_3$PO$_4$/NCDs was observed as compared to that of both Ag$_3$PO$_4$ and g-C$_3$N$_4$/Ag$_3$PO$_4$, indicating that the modification of Ag$_3$PO$_4$ by g-C$_3$N$_4$ and NCDs could accelerate interfacial electron transfer, and thus certain synergistic effect existed between these components. Under the visible light irradiation, a much smaller radius was obtained than that in the dark for all the samples, implying that the

impedance of the electrode was weakened due to the formation of photogenerated electrons and holes under the light irradiation, which is consistent with some previous reports [58,59]. All of above results confirm that the introduction of NCDs can obviously improve the transfer and separation of photogenerated carriers in g-C$_3$N$_4$/Ag$_3$PO$_4$/NCDs composites, and thus enhance the photocatalytic activity.

It is known that the ·O$_2$$^-$, h$^+$ and ·OH are the three major reactive species in photocatalytic reaction process [60]. In order to investigate the dominant active species in the photocatalytic process, the trapping experiments were carried out. As depicted in Fig. 7, benzoquinone (BZQ), disodium ethylenediaminetetraacetate (Na$_2$-EDTA) and isopropanol (IPA) are employed to act as ·O$_2$$^-$, h$^+$ and ·OH scavengers, respectively. Fig. 7a shows the photodegradation of MB with pure g-C$_3$N$_4$ photocatalyst after adding various trapping scavengers. It can be seen that the introduction of Na$_2$-EDTA or IPA into the system does not basically affect the photodegradation efficiencies of MB, but BZQ decreases the degradation efficiency greatly, which means that ·O$_2$$^-$ is the main reactive species in the g-C$_3$N$_4$ photocatalytic process. Fig. 7b shows the effects of different trapping scavengers on the Ag$_3$PO$_4$ photocatalyst. It is clear that h$^+$ acts as the dominant reactive species and ·OH also has a little effect on the photocatalytic efficiency. In contrast, the reactive species ·O$_2$$^-$ has almost no effect on the photocatalytic degradation. The effects of various scavengers on the binary g-C$_3$N$_4$/Ag$_3$PO$_4$ photocatalyst are shown in Fig. 7c. It can be seen that h$^+$ and ·OH play similar roles in g-C$_3$N$_4$/Ag$_3$PO$_4$ as them in Ag$_3$PO$_4$. However, the ·O$_2$$^-$ radicals also show an obvious effect on the photocatalysis of g-C$_3$N$_4$/Ag$_3$PO$_4$, suggesting the formation of Z-scheme heterojunction between g-C$_3$N$_4$ and Ag$_3$PO$_4$. Furthermore, as depicted in Fig. 7d, the effects of various scavengers on the photodegradation efficiencies of g-C$_3$N$_4$/Ag$_3$PO$_4$/NCDs are similar to those of g-C$_3$N$_4$/Ag$_3$PO$_4$, but with a further enhancement of ·O$_2$$^-$ radicals, suggesting that the introduction of NCDs into the g-C$_3$N$_4$/Ag$_3$PO$_4$ system can provide more oxygen defects, improving the oxygen activation ability.

In order to further elucidate the degradation mechanism, the ESR measurements of the photocatalysts were carried out. As shown in Fig. 8a, no signal of DMPO-·O$_2$$^-$ was found in the dark in the presence of g-C$_3$N$_4$/Ag$_3$PO$_4$/NCDs, proving no ·O$_2$$^-$ radicals were generated in the condition. In contrast, the four characteristic peaks of the DMPO-·O$_2$$^-$ adducts were observed over g-C$_3$N$_4$/Ag$_3$PO$_4$ and g-C$_3$N$_4$/Ag$_3$PO$_4$/NCDs under visible light irradiation. Moreover, the DMPO-·O$_2$$^-$ peaks over g-C$_3$N$_4$/Ag$_3$PO$_4$/NCDs are stronger than those over g-C$_3$N$_4$/Ag$_3$PO$_4$, indicating that more ·O$_2$$^-$ radicals were generated over g-C$_3$N$_4$/Ag$_3$PO$_4$/NCDs than g-C$_3$N$_4$/Ag$_3$PO$_4$. Since the O$_2$·$^-$ is generated via a one-electron reduction of O$_2$, the higher O$_2$·$^-$ intensity of g-C$_3$N$_4$/Ag$_3$PO$_4$/NCDs indicates that the enhanced molecular oxygen activation ability can be obtained by the introduction of NCDs. Similarly, no signal of DMPO·OH was detected in the dark (Fig. 8b). When exposed to visible light irradiation, a weak four-line ESR signal with an intensity ratio of 1:2:2:1 could be observed over Ag$_3$PO$_4$, g-C$_3$N$_4$/Ag$_3$PO$_4$ and g-C$_3$N$_4$/Ag$_3$PO$_4$/NCDs, indicating that ·OH species play a small role in

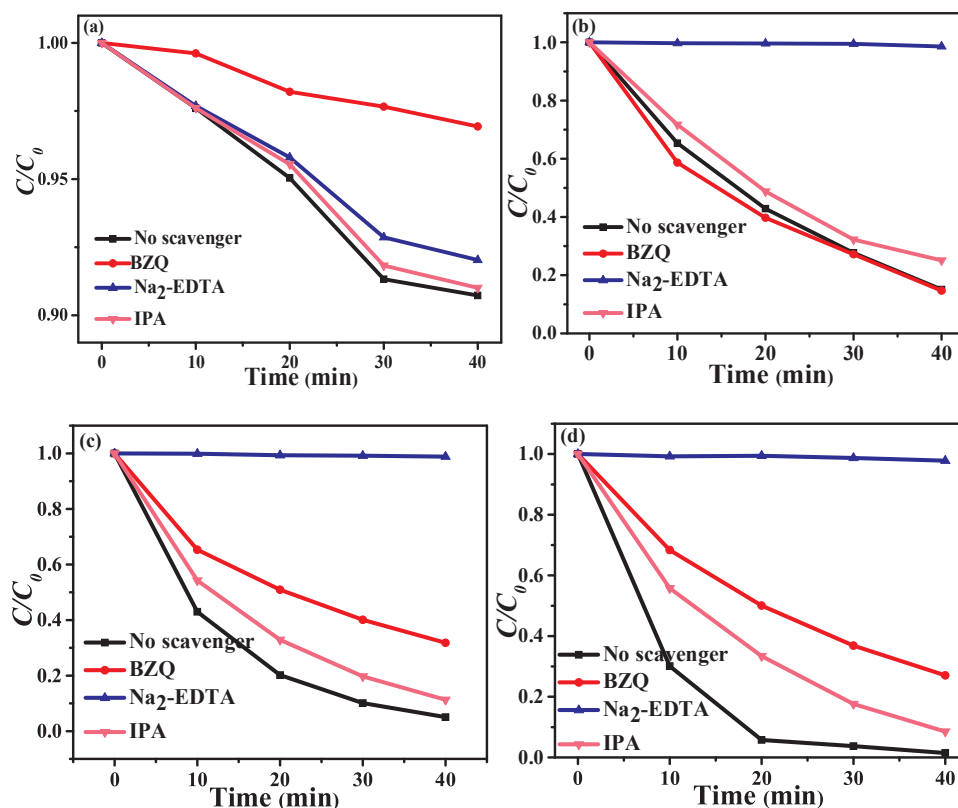**Fig. 7.** The trapping experiments of the active species for the photocatalytic reaction based on (a) g-C$_3$N$_4$, (b) Ag$_3$PO$_4$, (c) g-C$_3$N$_4$/Ag$_3$PO$_4$ and (d) g-C$_3$N$_4$/Ag$_3$PO$_4$/NCDs photocatalysts.

the photocatalytic processes of Ag$_3$PO$_4$, g-C$_3$N$_4$/Ag$_3$PO$_4$ and g-C$_3$N$_4$/Ag$_3$PO$_4$/NCDs. These results are well consistent with those of the trapping experiments.

For pure g-C$_3$N$_4$ with a band gap of 2.7 eV, the VB of g-C$_3$N$_4$ is estimated to be 1.4 eV and the CB is about −1.3 eV. The electrons produced on g-C$_3$N$_4$ are about −1.3 eV, which is more negative than −0.44 eV to reduce O$_2$ into ·O$_2^-$, as a result, ·O$_2^-$ species were generated to act as the main active species in the g-C$_3$N$_4$ photocatalytic process. For Ag$_3$PO$_4$ with a band gap of 2.45 eV, the VB is estimated to be 2.9 eV and the CB is about 0.45 eV. The electrons produced on Ag$_3$PO$_4$ are not negative enough to reduce O$_2$ to yield ·O$_2^-$ reactive species, so ·O$_2^-$ radicals has no effects in the Ag$_3$PO$_4$ photocatalytic system. For g-C$_3$N$_4$/Ag$_3$PO$_4$ and g-C$_3$N$_4$/Ag$_3$PO$_4$/NCDs photocatalysts, according to the trapping experiments and the DMPO spin-trapping ESR measurement, both h$^+$ and ·O$_2^-$ radicals are the main reactive species. Based on the above results, it is proposed that both binary g-C$_3$N$_4$/Ag$_3$PO$_4$ and ternary g-C$_3$N$_4$/Ag$_3$PO$_4$/NCDs could be Z-scheme photocatalysts.

The photocatalytic mechanism of the g-C$_3$N$_4$/Ag$_3$PO$_4$/NCDs

photocatalyst is shown in Fig. 9. Since Ag$_3$PO$_4$ particles were well anchored on g-C$_3$N$_4$ sheets, the photogenerated electrons in the CB of Ag$_3$PO$_4$ quickly transfer through the surface of g-C$_3$N$_4$ and combine with the holes in the VB of g-C$_3$N$_4$, leading to the accumulation of electrons in the CB of g-C$_3$N$_4$ and holes in the VB of Ag$_3$PO$_4$. Holes in the VB of Ag$_3$PO$_4$ would react with pollutants directly, and the electrons in the CB of g-C$_3$N$_4$ could reduce O$_2$ into ·O$_2^-$. When NCDs were introduced into the photocatalytic system, the enhanced photocatalytic activity can be ascribed to the following reasons. Firstly, the introduction of NCDs into the system enhances the light absorption ability due to their upconversion photoluminescence properties, leading to exciting g-C$_3$N$_4$ and Ag$_3$PO$_4$ to form more charge carriers, enhancing the photocatalytic activity of g-C$_3$N$_4$/Ag$_3$PO$_4$/NCDs; Secondly, due to the small size and excellent electron conductivity of NCDs, NCDs could serve as the charge transmission bridge between g-C$_3$N$_4$ and Ag$_3$PO$_4$, accelerating the combination of electrons on the CB of Ag$_3$PO$_4$ and holes on the VB of g-C$_3$N$_4$, which further enhances the photocatalytic performance. Thirdly, NCDs could act as both electron acceptors and donors, which make electrons easily transfer to the surface of g-C$_3$N$_4$

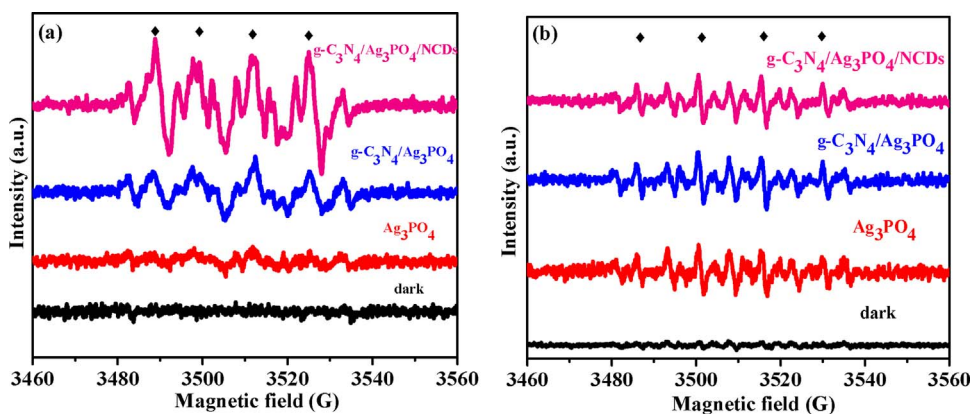**Fig. 8.** ESR spectra of (a) DMPO ·O$_2^-$ adducts in methanol solution and (b) DMPO ·OH adducts in aqueous solution recorded with g-C$_3$N$_4$, Ag$_3$PO$_4$, g-C$_3$N$_4$/Ag$_3$PO$_4$ and g-C$_3$N$_4$/Ag$_3$PO$_4$/NCDs under visible light irradiation.
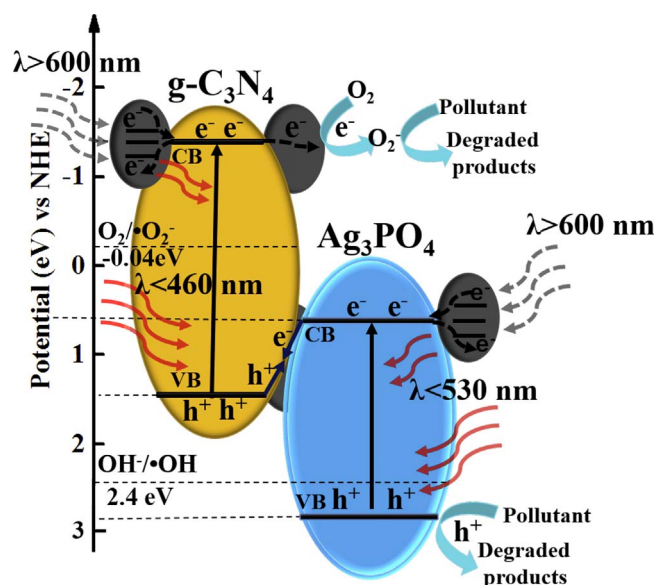
Fig. 9. Z-Scheme photocatalytic mechanism of g-C$_3$N$_4$/Ag$_3$PO$_4$/NCDs under visible-light irradiation.

and Ag$_3$PO$_4$ and the redundant electrons on g-C$_3$N$_4$ or Ag$_3$PO$_4$ can also be transferred to NCDs, which further improves the separation of electron-hole pairs; At last, after the NCDs were introduced into the system, high-energy electrons on the VB of g-C$_3$N$_4$ could directly transfer to the NCDs quickly and the well-separated electrons on the NCDs with intense reduction ability could react with O$_2$ to produce more ·O$_2^-$ reactive species [61], resulting in the improvement of the photocatalytic performance.

4. Conclusion

The g-C$_3$N$_4$/Ag$_3$PO$_4$/NCDs Z-scheme photocatalyst has been prepared by a facile two-step solution method. It exhibits excellent visible-light photocatalytic performance for MB, RhB and phenol degradation. The rate constant of g-C$_3$N$_4$/Ag$_3$PO$_4$/NCDs for MB degradation is as high as 0.1192 min^{-1}, which is 23.6, 2.6 and 1.6 times higher than that of g-C$_3$N$_4$ (0.00506 min^{-1}), Ag$_3$PO$_4$ (0.0463 min^{-1}) and g-C$_3$N$_4$/Ag$_3$PO$_4$ (0.0742 min^{-1}). The enhanced photocatalytic performance of g-C$_3$N$_4$/Ag$_3$PO$_4$/NCDs can be ascribed to the formation of Z-scheme heterojunction and more importantly, the existence of NCDs, which can accelerate electron transfer, enhance light harvesting capacity and improve molecular oxygen activation. This study further demonstrates that the development of NCDs inserted photocatalytsts could be a promising approach to high-performance visible-light driven photocatalysts.

Acknowledgements

Appendix A. Supplementary data

Supplementary data associated with this article can be found, in the online version, at https://doi.org/10.1016/j.apcatb.2018.01.057.

References

[1] Z. Zou, J. Ye, K. Sayama, H. Arakawa, Nature 414 (2001) 625–627.
[2] F.E. Osterloh, Chem. Soc. Rev. 42 (2013) 2294–2320.
[3] J. Zhu, F.T. Fan, R.T. Chen, H.Y. An, Z.C. Feng, C. Li, Angew. Chem. Int. Ed. 54 (2015) 9111–9114.
[4] H. Tada, T. Mitsui, T. Kiyonaga, T. Akita, K. Tanaka, Nat. Mater. 5 (2006) 782–786.
[5] S.Q. Song, A.Y. Meng, S.J. Jiang, B. Cheng, C.J. Jiang, Appl. Surf. Sci. 396 (2017) 1368–1374.
[6] K.L. He, J. Xie, X.Y. Luo, J.Q. Wen, S. Ma, X. Li, Y.P. Fang, X.C. Zhang, Chin. J. Catal. 38 (2017) 240–252.
[7] H. Tang, Y.H. Fu, S.F. Chang, S.Y. Xie, G.G. Tang, Chin. J. Catal. 38 (2017) 337–347.
[8] Z.H. Chen, W.L. Wang, Z.G. Zhang, X.M. Fang, J. Phys. Chem. C 117 (2013) 19346–19352.
[9] D. Ma, J. Wu, M.C. Gao, Y.J. Xin, Y.Y. Sun, T.J. Ma, Chem. Eng. J. 313 (2017) 1567–1576.
[10] A. Iwase, Y.H. Ng, Y. Ishiguro, A. Kudo, R. Amal, J. Am. Chem. Soc. 133 (2011) 11054–11057.
[11] X.L. Miao, X.P. Shen, J.J. Wu, Z.Y. Ji, J.H. Wang, L.R. Kong, M.M. Liu, C.S. Song, Appl. Catal. A 539 (2017) 104–113.
[12] X.C. Wang, K. Maeda, A. Thomas, K. Takanabe, G. Xin, J.M. Carlsson, K. Domen, M. Antonietti, Nat. Mater. 8 (2009) 76–80.
[13] H.Y. Lv, Z.Y. Teng, C.Y. Wang, G.X. Wang, Sens. Actuators B 242 (2017) 897–903.
[14] Z.Y. Teng, H.Y. Lv, C.Y. Wang, G.X. Wang, H.G. Xue, H. Pang, G.X. Wang, Carbon 113 (2017) 63–75.
[15] X.Q. Xie, K. Kretschmer, G.X. Wang, Nanoscale 7 (2015) 13278–13292.
[16] W.J. Ong, L.L. Tan, Y.H. Ng, S.T. Yong, S.P. Chai, Chem. Rev. 116 (2016) 7159–7329.
[17] Z.G. Yi, J.H. Ye, N. Kikugawa, T. Kako, S.X. Ouyang, H. Stuart-Williams, H. Yang, J.Y. Cao, W.J. Luo, Z.S. Li, Y. Liu, R.L. Withers, Nat. Mater. 9 (2010) 559–564.
[18] X.F. Yang, Z.P. Chen, J.S. Xu, H. Tang, K.M. Chen, Y. Jiang, ACS Appl. Mater. Interfaces 7 (2015) 15285–15293.
[19] C.F. Mu, Y. Zhang, W.Q. Cui, Y.H. Liang, Y.F. Zhu, Appl. Catal. B 212 (2017) 41–49.
[20] X.F. Yang, H. Tang, J.S. Xu, M. Antonietti, M. Shalom, ChemSusChem 8 (2015) 1350–1358.
[21] H.G. Yu, W.Y. Chen, X.F. Wang, Y. Xu, J.G. Yu, Appl. Catal. B 187 (2016) 163–170.
[22] Q.J. Xiang, D. Lang, T.T. Shen, F. Liu, Appl. Catal. B 162 (2015) 196–203.
[23] Y.M. He, L.H. Zhang, B.T. Teng, M.H. Fan, Environ. Sci. Technol. 49 (2015) 649–656.
[24] X.X. Chen, X.T. Huang, Z.G. Yi, Chem. Eur. J. 20 (2014) 17590–17596.
[25] S.G. Meng, X.F. Ning, T. Zhang, S.F. Chen, X.L. Fu, Phys. Chem. Chem. Phys. 17 (2015) 11577–11585.
[26] M. Ebrahimi, M. Samadi, S. Yousefzadeh, M. Soltani, A. Rahimi, T.C. Chou, L.C. Chen, K.H. Chen, A.Z. Moshfegh, ACS Sustain. Chem. Eng. 5 (2017) 367–375.
[27] S. Kumar, T. Surendar, A. Baruah, V. Shanker, J. Mater. Chem. A 1 (2013) 5333–5340.
[28] A.H. Zhao, J.M. Fan, W.H. Liu, Y.Q. Xue, S. Yin, J. Alloys Compd. 695 (2017) 2812–2819.
[29] J. Di, J.X. Xia, M.X. Ji, B. Wang, X.W. Li, Q. Zhang, Z.G. Chen, H.M. Li, ACS Sustain. Chem. Eng. 4 (2016) 136–146.
[30] W.J. Niu, R.H. Zhu, Y. Hua, H.B. Zeng, S. Cosnier, X.J. Zhang, D. Shan, Carbon 109 (2016) 402–410.
[31] P.J. Yang, J.H. Zhao, J. Wang, B.Y. Cao, L. Li, Z.P. Zhu, J. Mater. Chem. A 3 (2015) 8256–8259.
[32] J. Liu, Y. Liu, N.Y. Liu, Y.Z. Han, X. Zhang, H. Huang, Y. Lifshitz, S.T. Lee, J. Zhong, Z.H. Kang, Science 347 (2015) 970–974.
[33] J. Tian, Y.H. Leng, Z.H. Zhao, Y. Xia, Y.H. Sang, P. Hao, J. Zhan, M.C. Li, H. Liu, Nano Energy 11 (2015) 419–427.
[34] H. Yu, H.C. Zhang, H. Huang, Y. Liu, H.T. Li, H. Ming, Z.H. Kang, New J. Chem. 36 (2012) 1031–1035.
[35] Y.Q. Zhang, D.K. Ma, Y.G. Zhang, W. Chen, S.M. Huang, Nano Energy 2 (2013) 545–552.
[36] S.N. Baker, G.A. Baker, Angew. Chem. Int. Ed. 49 (2010) 6726–6744.
[37] Q. Han, B. Wang, J. Gao, Z.H. Cheng, Y. Zhao, Z.P. Zhang, L.T. Qu, ACS Nano 10 (2016) 2745–2751.
[38] X.L. Miao, Z.Y. Ji, J.J. Wu, X.P. Shen, J.H. Wang, L.R. Kong, M.M. Liu, C.S. Song, J. Colloid Interface Sci. 502 (2017) 24–32.
[39] S.J. Zhu, Q.N. Meng, L. Wang, J.H. Zhang, Y.B. Song, H. Jin, K. Zhang, H.C. Sun, H.Y. Wang, B. Yang, Angew. Chem. Int. Ed. 52 (2013) 3953–3957.
[40] H.Y. Li, S.Y. Gan, H.Y. Wang, D.X. Han, L. Niu, Adv. Mater. 27 (2015) 6906–6913.
[41] S. Bai, X.P. Shen, H.W. Lv, G.X. Zhu, C.L. Bao, Y.X. Shan, J. Colloid Interface Sci. 405 (2013) 1–9.
[42] J. Jiang, O.Y. Lei, L. Zhu, A. Zheng, J. Zou, X. Yi, H. Tang, Carbon 80 (2014) 213–221.
[43] Q.J. Xiang, J.G. Yu, M. Jaroniec, J. Phys. Chem. C 115 (2011) 7355–7363.
[44] J. Ding, W. Xu, H. Wan, D.S. Yuan, C. Chen, L. Wang, G.F. Guan, W.L. Dai, Appl. Catal. B 221 (2018) 626–634.
[45] J.J. Wu, X.P. Shen, X.L. Miao, Z.Y. Ji, J.H. Wang, T. Wang, M.M. Liu, Eur. J. Inorg. Chem. 21 (2017) 2845–2853.
[46] J. Yan, C. Wang, H. Xu, Y.G. Xu, X.J. She, J.J. Chen, Y.H. Song, H.M. Li, Q. Zhang, Appl. Surf. Sci. 287 (2013) 178–186.
[47] Ch. Fettkenhauer, G. Clavel, M. Kailasam, M. Antonietti, D. Dontsova, Green Chem. 17 (2015) 3350–3361.
[48] C. Cui, S. Li, Y.W. Qiu, H.H. Hu, X.Y. Li, C.R. Li, J.K. Gao, W.H. Tang, Appl. Catal. B

200 (2017) 666–672.

[49] L. Zhou, W. Zhang, L. Chen, H.P. Deng, J. Colloid Interface Sci. 487 (2017) 410–417.

[50] S. Nayak, L. Mohapatra, K. Parida, J. Mater. Chem. A 3 (2015) 18622–18635.

[51] C. Cui, Y.P. Wang, D.Y. Liang, W. Cui, H.H. Hu, B.Q. Lu, S. Xu, X.Y. Li, C. Wang, Y. Yang, Appl. Catal. B 158–159 (2014) 150–160.

[52] F.J. Zhang, F.Z. Xie, S.F. Zhu, J. Liu, J. Zhang, S.F. Mei, W. Zhao, Chem. Eur. J. 228 (2013) 435–441.

[53] G.A.M. Hutton, B.C.M. Martindale, E. Reisner, Chem. Soc. Rev. 46 (2017) 6111–6123.

[54] J. Schneider, C.J. Reckmeier, Y. Xiong, M. Von Seckendorff, A.S. Susha, P. Kasak, A.L. Rogach, J. Phys. Chem. C 121 (2017) 2014–2022.

[55] F.M. Huang, C. Li, H.L. Wang, Z.C. Yan, Chem. Eur. J. 62 (2010) 250–256.

[56] J.W. Lin, X.L. Weng, X.Y. Jin, M. Megharaj, R. Naidu, Z.L. Chen, RSC Adv. 5 (2015) 70874–70882.

[57] J. Di, J.X. Xia, M.X. Ji, B. Wang, S. Yin, Y. Huang, Z.G. Chen, H.M. Li, Appl. Catal. B 188 (2016) 376–387.

[58] L. Liu, Y.H. Qi, J.R. Lu, S.L. Lin, W.J. An, Y.H. Liang, W.Q. Cui, Appl. Catal. B 183 (2016) 133–141.

[59] F. Chen, Q. Yang, S.N. Wang, F.B. Yao, J. Sun, Y.L. Wang, C. Zhang, X.M. Li, C.G. Niu, D.B. Wang, G.M. Zeng, Appl. Catal. B 209 (2017) 493–505.

[60] M. Pelaez, A.A. Cruz, K. O'Shea, P. Falaras, D.D. Dionysiou, Water Res. 45 (2011) 3787–3796.

[61] J. Di, J.X. Xia, X.L. Chen, M.X. Ji, S. Yin, Q. Zhang, H.M. Li, Carbon 114 (2017) 601–607.